




Rupture Process During the 2015 Illapel, Chile Earthquake: Zigzag-Along-Dip Rupture Episodes

RYO OKUWAKI,¹  YUJI YAGI,² RAFAEL ARÁNGUIZ,^{3,4} JUAN GONZÁLEZ,^{4,5} and GABRIEL GONZÁLEZ^{4,5}

Abstract—We constructed a seismic source model for the 2015 M_W 8.3 Illapel, Chile earthquake, which was carried out with the kinematic waveform inversion method adopting a novel inversion formulation that takes into account the uncertainty in the Green's function, together with the hybrid backprojection method enabling us to track the spatiotemporal distribution of high-frequency (0.3–2.0 Hz) sources at high resolution by using globally observed teleseismic P-waveforms. A maximum slip amounted to 10.4 m in the shallow part of the seismic source region centered 72 km northwest of the epicenter and generated a following tsunami inundated along the coast. In a gross sense, the rupture front propagated almost unilaterally to northward from the hypocenter at <2 km/s, however, in detail the spatiotemporal slip distribution also showed a complex rupture propagation pattern: two up-dip rupture propagation episodes, and a secondary rupture episode may have been triggered by the strong high-frequency radiation event at the down-dip edge of the seismic source region. High-frequency sources tends to be distributed at deeper parts of the slip area, a pattern also documented in other subduction zone megathrust earthquakes that may reflect the heterogeneous distribution of fracture energy or stress drop along the fault. The weak excitation of high-frequency radiation at the termination of rupture may represent the gradual deceleration of rupture velocity at the transition zone of frictional property or stress state between the megathrust rupture zone and the swarm area.

Key words: 2015 Illapel Chile earthquake, Source process, Kinematic waveform inversion, Hybrid backprojection, Subduction zone earthquake, Along-dip rupture propagation.

Electronic supplementary material The online version of this article (doi:10.1007/s00024-016-1271-6) contains supplementary material, which is available to authorized users.

¹ Graduate School of Life and Environmental Sciences, University of Tsukuba, 1-1-1 Tennodai, Tsukuba, Ibaraki 3058572, Japan. E-mail: rokuwaki@geol.tsukuba.ac.jp

² Faculty of Life and Environmental Sciences, University of Tsukuba, 1-1-1 Tennodai, Tsukuba, Ibaraki 3058572, Japan.

³ Department of Civil Engineering, Universidad Católica de la Sma Concepción, Alonso de Ribera 2850, Concepción, Chile.

⁴ Centro Nacional de Investigación para la Gestión Integrada de Desastres Naturales, CONICYT/FONDAP/1511007, Santiago, Chile.

⁵ Departamento de Ciencias Geológicas, Universidad Católica del Norte, Avenida Angamos 0610, Antofagasta, Chile.

1. Introduction

A great earthquake affected the coastal area of north central Chile on 16 September 2015 at local time 19:54:31 (UTC 22:54:31). According to the information from the Centro Sismológico Nacional, Universidad de Chile (CSN: <http://www.sismologia.cl>, last accessed on 16 November 2015), the moment magnitude was estimated at M_W 8.4, and the coast near the source region experienced the severe shaking (the maximum Mercalli intensity scale of VIII was observed in the Coquimbo region). The hypocentral location determined by the CSN is 31.637°S, 71.741°W (54 km west of Illapel city) at 23.3 km depth, and the focal mechanism determined by the Global Centroid Moment Tensor project (GCMT: <http://www.globalcmt.org/CMTsearch.html>, last accessed on 16 November 2015) represents a low-angle thrust faulting (Fig. 1), indicating that the 2015 Illapel earthquake occurred along the interface of the plate boundary where the Nazca plate is subducting beneath the South America plate at a rate of about 74 mm/year (DeMETS *et al.* 2010; Fig. 1). Following the mainshock, a tsunami struck the coast with a significant impact near the source region. A narrow continental shelf dominated by abrupt coastal cliff morphology characterizes the area. The post-tsunami surveys showed that the tsunami run-ups varied from 3 to 6 m with a decaying trend at both sides of the source area, and the maximum run-up was observed at Totoral village (30.365°S, 71.670°W; Fig. 1), where it reached 10.8 m discounting splashing up (ARÁNGUIZ *et al.* 2016).

The source region of the 2015 Illapel earthquake is part of the seismically active Coquimbo-Illapel region (30°–32°S). The greatest historical Chilean earthquake covering this area was the 1730

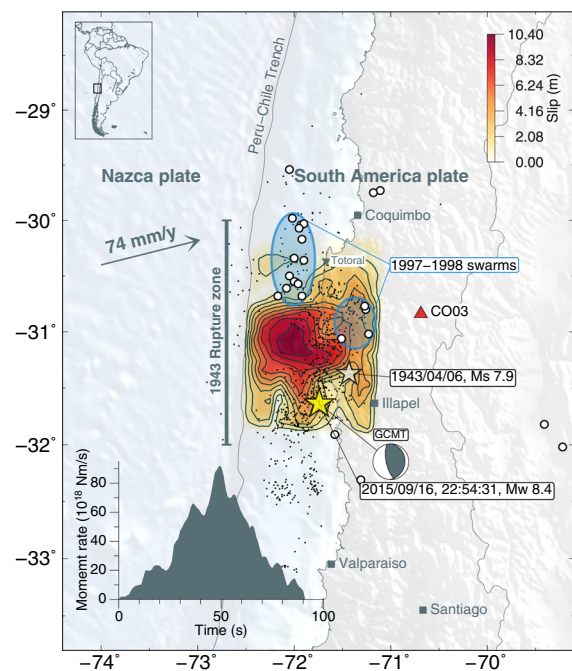


Figure 1

Yellow, and white stars represent the epicenters of the 2015 Illapel earthquake determined by the CSN and the 1943 Illapel earthquake fetched from the Centennial Catalog (ENGDahl and VILLASEÑOR 2002), respectively. Contours show the slip distribution every 1.04 m. Black dots correspond to the 1-week-aftershock epicenters matching criteria of $M \geq 3$ and shallower than 50 km depth, determined by the CSN. Inset graph shows the moment-rate function obtained by the inversion analysis. Beach ball represents the focal mechanism determined by the GCMT project. Vertical bar represents the estimated rupture length of the 1943 Illapel earthquake (BECK *et al.* 1998). Arrow indicates the motion of the Nazca plate relative to the fixed South America plate employing the MORVEL model (DEMETTS *et al.* 2010). Blue-rimmed areas represent the 1997–1998 swarms (LEMOINE and MADARIAGA 2001), and open black circles are the relocated epicenters of the 1997–1998 swarms in the magnitude range $5.5 \leq mb \leq 6.2$ (PARDO *et al.* 2002). Red triangle depicts the location of the station CO03 providing the strong motion record illustrated in Supplementary Figure S9. Background topography and bathymetry are from ETOPO1 (AMANTE and EAKINS 2009)

earthquake whose magnitude is estimated to be M_S 8.5–9 (LOMNITZ 2004), and its rupture area is estimated to be extended from Coquimbo (30°S) down to the northern part (35°S) of the rupture zone of the 2010 Maule, Chile, earthquake (e.g., UDIAS *et al.* 2012). The last significant earthquake in this region, but much smaller than the 1730 earthquake, was the M_S 7.9 1943 Illapel earthquake (Centennial Catalog; ENGDahl and VILLASEÑOR 2002), and its source region

estimated by BECK *et al.* (1998) overlaps the rupture area of the 2015 Illapel earthquake (Fig. 1). After the occurrence of the 1943 Illapel earthquake, the seismic gap in the Coquimbo-Illapel region was partially reactivated during 1997–1998 by two-clustered swarms (LEMOINE and MADARIAGA 2001; PARDO *et al.* 2002) occurred along the plate interface located north and east of the source region of the 2015 Illapel earthquake (Fig. 1). GARDI *et al.* (2006) found that the 1997–1998 swarms can be explained as a result of the stress transfer from the aseismic slip (~ 65 mm/year) below the down-dip edge of the seismogenic zone. MORENO *et al.* (2010), using the global positioning system (GPS) data from 1996–2008, found that the plate interface in the middle part of the Coquimbo-Illapel region is strongly locked (almost 100 % coupled), making it the potential site of a future earthquake. MÉTOIS *et al.* (2014) also used the GPS data to invert a degree of interplate coupling and showed that the middle to southern part of the Coquimbo-Illapel region is almost 100 % coupled at 15–25 km depth, while the coupling at northern part is relatively low, which corresponds to the northern part of the 1997–1998 swarm region. Considering the swarm activity and the plate-locking distribution along the Coquimbo-Illapel region, the 2015 Illapel earthquake occurred where the stress build-up has progressed non-uniformly in both space and time since the 1943 Illapel earthquake.

This study aims to investigate a detailed rupture history during the 2015 Illapel earthquake. To construct a seismic source model, we estimated the spatiotemporal distribution of slip and high-frequency (0.3–2.0 Hz) sources by using the kinematic waveform inversion method that takes into account the uncertainty in Green's function (YAGI and FUKAHATA 2011) together with the HBP method (YAGI *et al.* 2012; OKUWAKI *et al.* 2014) to track the spatiotemporal distribution of high-frequency sources, respectively. Our integrated approach, using a wide range of frequency contents in the P-waveforms, is essential for tracking the rupture propagation history in detail because the high-frequency waves (~ 1 Hz) are generated by abrupt changes in the rupture velocity and/or slip-rate (e.g., MADARIAGA 1977; BERNARD and MADARIAGA 1984; SPUDICH and FRAZER 1984), and the high-frequency signal can be an index

of the rapid change of rupture behavior that is difficult to be detected from low frequency waveforms (OKUWAKI *et al.* 2014; YAGI and OKUWAKI 2015). By comparing the distribution of inverted slip and high-frequency sources, we propose an integrated seismic source model involving two rupture episodes characterized by along-dip rupture propagation at variable rupture speeds.

2. Data and Methods

We downloaded 42 teleseismic, vertical component of P-waveforms through the Incorporated Research Institutions for Seismology–Data Management Center (IRIS-DMC; Fig. 2a). The data were selected to ensure good azimuthal coverage and high signal-to-noise ratios. The first rise of the P-phase on each seismogram was manually picked (Fig. 2b), and we excluded the data whose P-phase is difficult to be reliably picked (See examples of the excluded waveforms in Supplementary Figure S8). The instrument response of each waveform was deconvolved to velocity with the sampling rates of 0.05 s for the HBP analysis and 1.0 s for the inversion analysis. The data were then, filtered into frequency bands of 0.3–2.0 Hz for the HBP analysis and 0.001–0.36 Hz for the inversion analysis.

The HBP method (a basic principle of this method and a sensitivity test are provided in Supplementary Text S2 and Figure S6) can track the spatiotemporal evolution of high-frequency radiation sources by stacking cross-correlation functions of the observed waveform and the Green's function. The HBP method improves upon the backprojection (BP) method (ISHII *et al.* 2005; KRÜGER and OHRNBERGER 2005) in two ways: it can mitigate the systematic delay of projected images of high-frequency sources distorted by the depth phases (pP and sP phases), and by using globally observed waveforms it can produce higher-resolution images than array-based BP methods (e.g., WALKER *et al.* 2005; OKUWAKI *et al.* 2014; FAN and SHEARER 2015). The HBP method can be useful for capturing the rupture front velocity, rupture direction, and rupture extents as it does not require values of these characteristics to be assumed before processing, and the information of rupture behaviors

from the HBP method can be used as constraint conditions for the kinematic waveform inversion (OKUWAKI *et al.* 2014).

Kinematic waveform inversion methods have been developed since 1980s (e.g., OLSON and APSEL 1982; HARTZELL and HEATON 1983) and applied to the numerous earthquakes to resolve a spatiotemporal behavior of rupture propagation. We adopted YAGI and FUKAHATA (2011)'s inversion formulation (a methodology is documented in Supplementary Text S1), which can mitigate the effect of uncertainty in the Green's function, a major source of modeling errors in waveform inversion procedures that has resulted in non-uniqueness of seismic source models for the same earthquake by different researchers (e.g., BERESNEV 2003). Since the strength of smoothing constraint for the spatiotemporal distribution of the model parameters and the data covariance matrix including the uncertainty in Green's function are objectively determined by minimizing the Akaike's Bayesian information criterion (ABIC, AKAIKE 1980), the information of the observed data limits the maximum amount of the inverted slip in this formulation.

For both the HBP and the inversion analyses, the fault geometry was constructed with the constant strike and dip angles being 2.7° and 15.0°, respectively, based on the W phase source inversion by Duputel *et al.* (http://wphase.unistra.fr/events/illapel_2015/index.html, last accessed on 16 November 2015) and the slab geometry around the source region (HAYES *et al.* 2012; TASSARA and ECHAUREN 2012). The initial rupture point adopted (assumed hypocenter) was the CSN epicenter of 31.637°S, 71.741°W, and 25 km depth. For the HBP analysis, the rake angle on each source node was assumed pure thrust motion relative to the plate-motion direction, referring the MORVEL model (DEMETTS *et al.* 2010). The validity of assumption of the rake angle is tested against the variable rake angles interpolated from the inversion result (see Supplementary Figure S7). From a simple observation of the teleseismic records, there is a clear directivity of rupture toward northern azimuth (Supplementary Figure S10), and the aftershocks during 1 week following the main shock are densely distributed around and northern part of the epicenter (Fig. 1). Preliminary HBP and the BP results hitherto published (YE *et al.* 2016; MELGAR

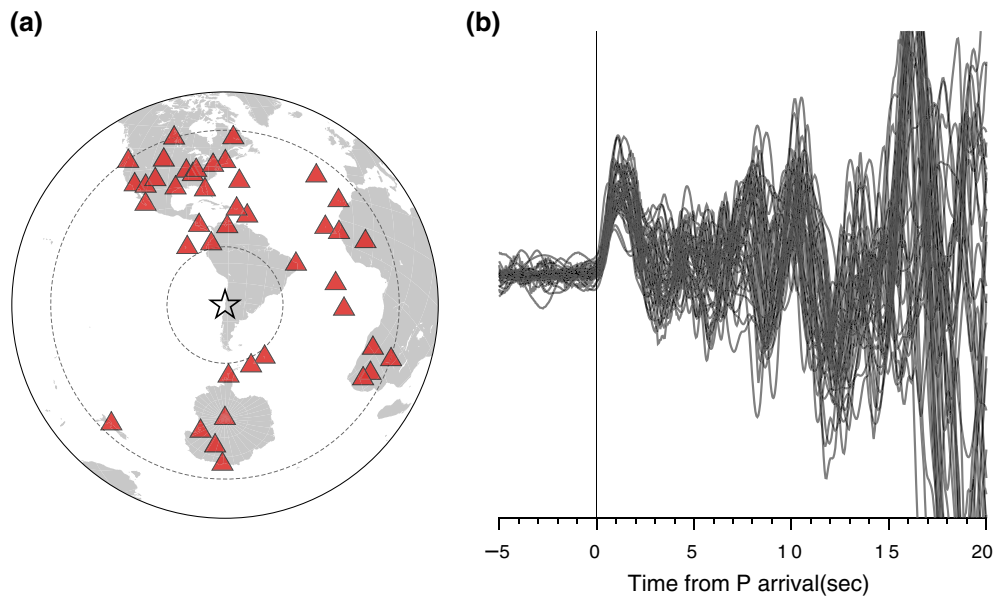


Figure 2

a Distribution of teleseismic stations used for both the waveform inversion and the HBP analyses. *Star* and *triangles* represent the CSN epicenter and the teleseismic stations, respectively. *Dotted lines* indicate the teleseismic distances of 30° and 90° . **b** Traces of vertical component of unfiltered P-waveforms used in both the inversion and the HBP analyses. Each trace is normalized by its maximum absolute amplitude. The *abscissa* represents the time relative to the first arrival of P-phase

et al. 2016) indicate that the high-frequency signals are located northern part of the epicenter. Guided by this information, total available rupture area for both the inversion and the HBP analyses is assumed 190 km length and 130 km width, and the initial rupture point is set at 30 km from the southern edge of the fault model. A maximum rupture velocity for the inversion analysis is assumed 1.8 km/s based on the preliminary HBP analysis, and the alternative results assuming various maximum rupture velocities are provided in Supplementary figures S3 and S4. The source node interval along strike and dip directions were 2 km by 2 km for the HBP analysis and 10 km by 10 km for the inversion analysis. For the inversion analysis, a slip-rate function on each source node was represented as linear B-splines with a time length of 35 s and a time interval of 1.0 s, and the total source duration was 90 s. Green's functions were calculated based on the method of KIKUCHI and KANAMORI (1991). We used the local velocity structure (Supplementary Table S1) derived from the tomographic 2-D velocity-depth model of CONTRERAS-REYES *et al.* (2014) and the CRUST1.0 model

(LASKE *et al.* 2013) for calculating the Haskell propagator matrix in Green's function, and also used the ak135 model (KENNETT *et al.* 1995) for calculating the travel times, geometrical spreading factors, and ray parameters.

3. Results

The total slip distribution and the seismic moment release rate are shown in Fig. 1. The slip vectors inferred from the waveform inversion represent the typical thrust motion against the plate convergence (Fig. S1). Large slip is focused on shallow, up-dip portion of the fault plane where a large slip patch is centered 72 km northwest of the epicenter. The total seismic moment release was 3.3×10^{21} Nm (M_W 8.3). Slight difference in the seismic moment from other study (e.g., 2.67×10^{21} Nm, YE *et al.* 2016) may come from the variation in fault geometry and slip locations along the dip direction since the seismic moment depends on assumed rigidity and the rigidity increases with depth.

Figure 3 shows the spatiotemporal distribution of slip-rate and high frequency sources, and we project the Fig. 3 into the strike (Fig. 4a) and dip directions (Fig. 4b) to present the details of the rupture propagation history. For the first 25 s, the rupture initiated at the hypocenter and propagated mainly up-dip; northwestward at the speed of 2 km/s, and the area of large slip-rate was centered 16 km northwest of the epicenter. From 30 s after the initiation of rupture, the rupture front started propagating from the down-dip portion at 60 km northeast of the epicenter. It then propagated up-dip into the shallow part of the fault plane, and the largest slip occurred at 50 s centered 72 km northwest of the epicenter, where the seismic moment release rate reached a peak of 8.8×10^{19} Nm/s. The slip gradually declined at shallow part of the fault plane until it terminated at 90 s.

Spatiotemporal distribution of high-frequency sources shows that relatively weak strength of high-frequency sources initially propagated down-dip, northeast of the epicenter, and then returned to the up-dip portion of the fault plane at the speed of 2 km/s (Fig. 4b). From 20 s, the high-frequency sources started propagating down-dip again at the speed of 3 km/s along the dip direction, and at 25–27 s the relatively strong high-frequency radiation was observed at 60 km northeast of the epicenter. From 30 s to 90 s, high-frequency sources seemed to propagate up-dip at the speed of about 3 km/s along the dip direction (Fig. 4b). The strength of high-frequency sources is relatively weak at this sequence, and the high-frequency radiation ceased after 80 s.

4. Discussion

The seismic source model, which integrates the inverted slip together with the high-frequency sources, shows that the rupture process involves two distinct episodes of rupture propagation, which are divided into the first 25 s from the hypocentral time and the following ruptures. In the first sequence (0–25 s), rupture mainly propagates up-dip to the northwest of the epicenter at the rupture front velocity <2 km/s, and temporarily terminates at about 16 km northwest of the epicenter. High-frequency sources

generally follow the rupture front edges, but are distributed mainly at the deeper parts of the slip. During the second sequence (25–90 s), rupture starts propagating up-dip from the down-dip part of the fault plane, after the excitation of the relatively strong high-frequency radiation at ~ 27 s. This burst of the high-frequency signals, shown in the panel of 26–30 s in Fig. 3, is consistent with the rise of the moment-rate function at around 25 s (Fig. 1). The propagation speed of rupture front varies along the strike and dip directions. The rupture speed along the strike direction (Fig. 4a) is estimated to be <2 km/s, which is the same as in the first rupture sequence, but the rupture velocity along the dip direction is relatively fast, exceeding 3 km/s (Fig. 4b). The two rupture episodes observed from the analyses of teleseismic records are also confirmed by looking at the strong motion record at CO03 station, located at 134 km northeast of the epicenter (see Supplementary Figure S9). The strong motion record indicates the modest amplitude of waves at the first rupture episode continuing about 15 s from the onset of the first P-phase, and the following intense, large amplitude at the second rupture episode. Similarity of the initial rupture phase followed by the intense secondary rupture event can be recognized during the 2014 Iquique (Pisagua), Chile, earthquake (e.g., YAGI *et al.* 2014; RUIZ *et al.* 2014), while the clear intense foreshock activity, which is the remarkable feature of the 2014 Iquique earthquake, has not been reported for the 2015 Illapel earthquake.

The switch from the first to the second rupture episodes is marked by the strong high-frequency radiation at the down-dip edge of the slip area below the coast. Theoretical studies show that high-frequency waves are generated by abrupt changes in rupture velocity and/or slip-rate (e.g., MADARIAGA 1977; BERNARD and MADARIAGA 1984; SPUDICH and FRAZER 1984), and SPUDICH and FRAZER (1984) concluded that it is difficult to distinguish which factor, discontinuity in rupture velocity or slip-rate, could be the main generator of high-frequency waves. OHNAKA and YAMASHITA (1989) also shows that slip-rate increases as the rupture velocity accelerates and diverges if the rupture velocity equals to shear wave velocity for the anti-plane crack, and Rayleigh wave velocity for the in-plane crack. Although we cannot

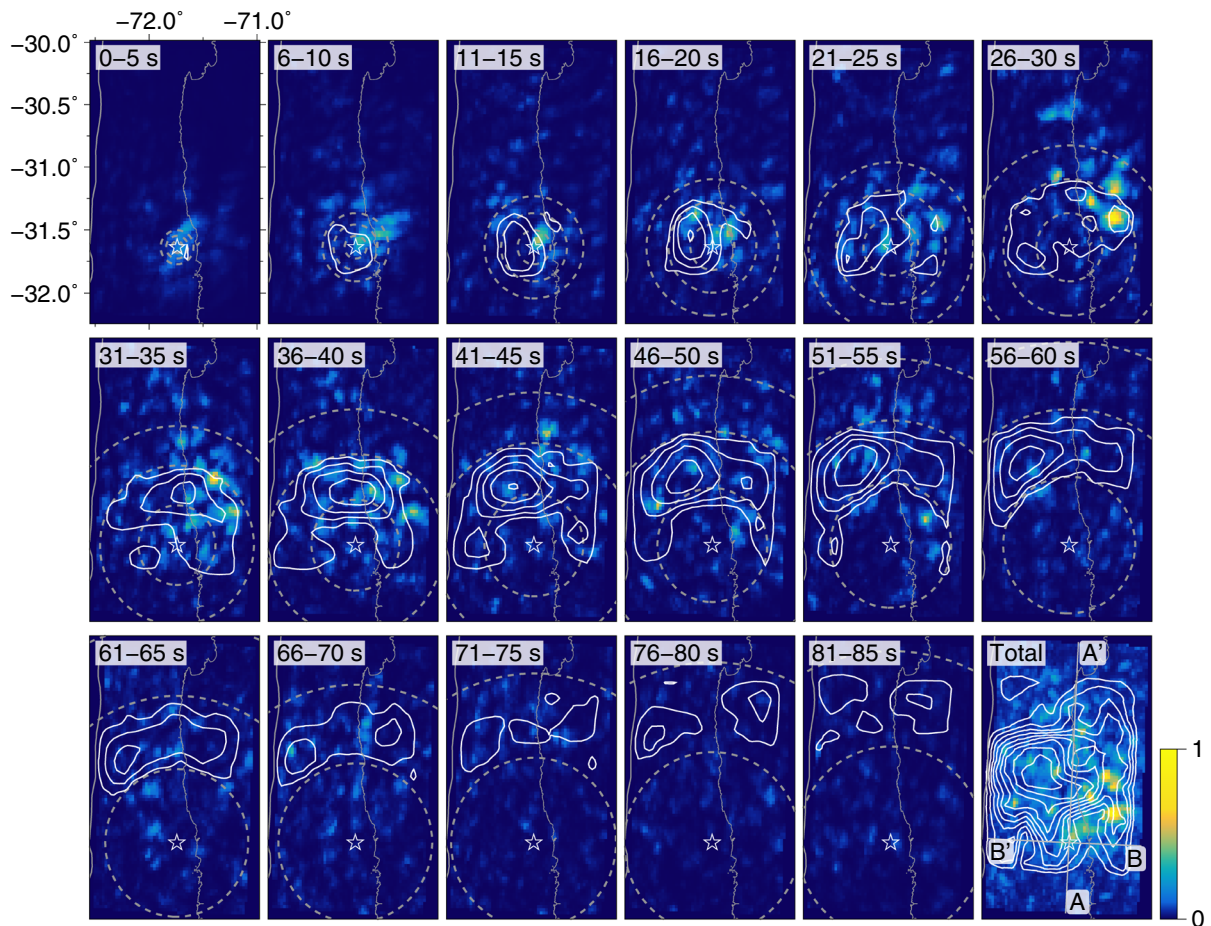


Figure 3

Snapshots of spatial distribution of inverted slip-rate and high-frequency sources every 5 s. The *right-bottom panel* is the total distribution. *Background color* represents the normalized strength of high-frequency radiation sources obtained by the HBP analysis. *White contours* are the slip-rate distribution every 0.11 m/s and the total slip distribution every 1.04 m for the *right-bottom panel*. *Dotted lines* are the constant expanding-rupture speeds from the hypocenter along the fault plane of 1, 2, and 3 km/s. *Star* denotes the CSN epicenter. *Top-left numbers* on each snapshot indicates the time window. *Lines A–A'* and *B–B'* on the *right-bottom panel* are the projection line along the strike and dip directions, respectively, which are used for generating Fig. 4

see a clear propagation path from the first to the second rupture episode, the strong high-frequency radiation at the down-dip edge of the slip area may reflect the acceleration of the slip-rate or rupture velocity that could have triggered the second rupture sequence that produced the large slip. Such an interaction between the preceding strong high-frequency radiation and the following large asperity rupture is also observed during the M_W 8.8 2010 Maule, Chile earthquake (OKUWAKI *et al.* 2014).

In both rupture episodes, high-frequency sources tend to be distributed at a deeper part of the slip

distribution, and the strength of high-frequency sources is relatively weak in areas of ongoing large slip. The same association of high-frequency sources and the slip (inverted from low frequency waveforms) has been documented during the M_W 8.8 2010 Maule, Chile earthquake (OKUWAKI *et al.* 2014) using the same methodology as this study, as well as for the 2015 Illapel earthquake (YE *et al.* 2016; MELGAR *et al.* 2016), and other subduction zone megathrust earthquakes (e.g., KOPER *et al.* 2011; LAY *et al.* 2012). Theoretical studies suggest that spatial heterogeneity of fracture energy or stress drop induces

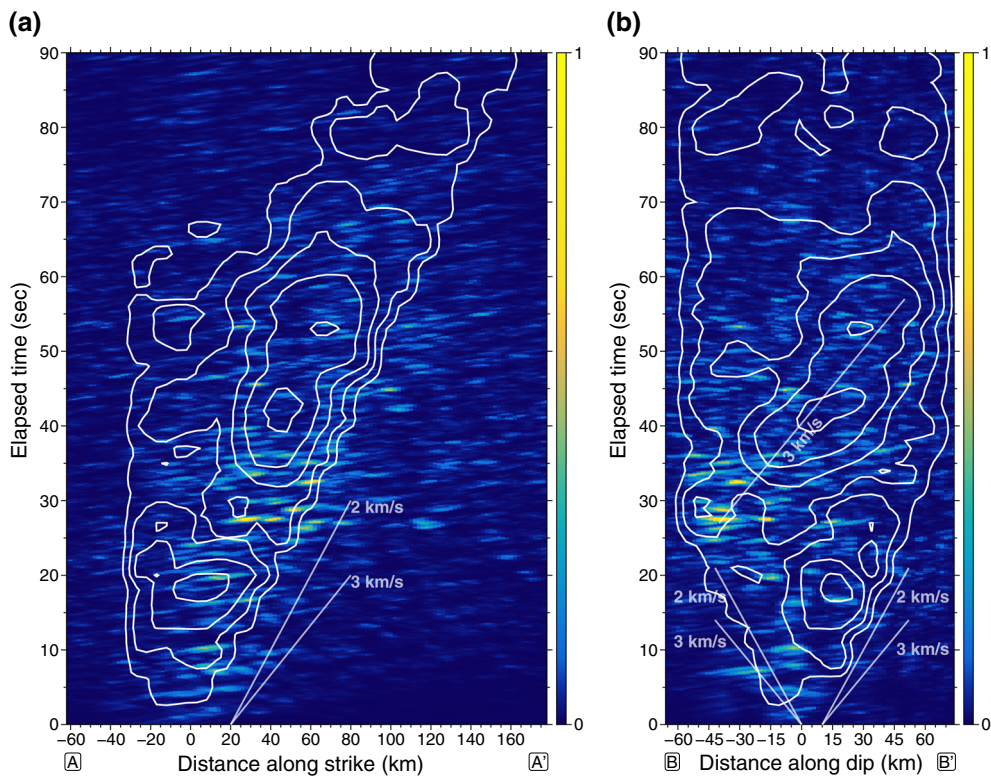


Figure 4

Time evolution of the slip-rate and the high-frequency sources along (a) the strike and (b) dip directions. *Abscissa* represents the distance from the epicenter along (a) the strike and (b) dip directions. *Ordinate* is the elapsed time from the hypocentral time. *Solid lines* are the reference rupture speeds. *Background color* and *contour interval* is the same as Fig. 3

discontinuities in rupture propagation (e.g., HUSSEINI 1975; FUKUYAMA and MADARIAGA 1998), which in turn generates high-frequency waves (e.g., SPUDICH and FRAZER 1984). Hence, our source model may reflect the heterogeneous distribution of fracture energy or stress drop along the fault.

Other prominent feature of the integrated rupture history can be highlighted at the termination of the second rupture episode (60–90 s), where slip-rate gently declines from about 60 s, and high-frequency sources are almost absent. This tendency is contrary to what is observed during the 2015 Gorkha, Nepal, earthquake, where the rupture front velocity abruptly decelerates and it generates strong high-frequency radiation as a stopping phase (e.g., MADARIAGA 1977) at the end of the rupture sequence (YAGI and OKUWAKI 2015). The northern edge of the 2015 Illapel source region coincides with the transition zone between high and low coupled region (MORENO *et al.* 2010;

MÉTOIS *et al.* 2014) and the southern edge of the 1997–1998 swarms (Fig. 1). HOLTkamp and BRUDZINSKI (2014) argued that the megathrust rupture often terminates around the swarm region due to the spatial variation of the stress regime, and the swarm activity may act as a proxy for the segmentation of the megathrust rupture. The weak excitation of high-frequency radiation at the terminal of rupture may reflect gradual rupture deceleration (e.g., SPUDICH and FRAZER 1984), and this gradual-rupture-stopping behavior might suggest that the rupture front penetrates into the swarm dominated region, where the significant change in frictional property or stress state may exist (e.g., KANEKO *et al.* 2010). However, as it can be seen in the sensitivity test for the HBP method (Supplementary Figure S6), the strength of response from the multiple synthetic point sources at the shallower part of the fault is, in general, at most 30–40 % weaker than that at the

deeper part. Even considering this imaging artifact in the synthetic test, the strength of the observed signals at around the terminus of the second rupture episode (60–90 s) is still weaker than that of the strong high-frequency signals observed at the initiation of the second rupture episode at the down-dip edge of the slip, and this artifact does not significantly affect the validity of the discussion.

Slip distribution inferred from the waveform inversion analysis correlates well with the highly locked region in the plate-coupling models by MORENO *et al.* (2010) and MÉTOIS *et al.* (2014). The locations of the 1997–1998 swarms coincide with the northern and northeastern edges of the slip area (Fig. 1), and for at least 5 years before the 2015 Illapel earthquake, seismicity around and south of the epicenter (from the CSN earthquake catalog) was more active than in the rest of the source region (Fig. S11). These pre-seismic activities outline the source region of the 2015 Illapel earthquake and may have had a role in determining the area favorable to rupture. However, the slip deficit amounts to 5.3 m if assuming 100 % coupled from the 1943 earthquake, while the maximum inverted slip is much larger than 5.3 m (Fig. 1). Although the peak slip amplitude is slightly fluctuated by the assumption of the maximum rupture velocity (Supplementary Figure S3), the slip deficit is still much less than the amount of inverted slip. We believe that the slip deficit since the 1943 earthquake is not enough for the occurrence of the 2015 event, and some amounts of slip deficit further before the 1943 earthquake should be necessary. Moreover, the surveys of tsunami-affected field have suggested that there are spatial differences between tsunami inundation areas along the coast between the 1943 and the 2015 Illapel earthquakes (ARÁNGUIZ *et al.* 2016). Thus, the 2015 Illapel earthquake is not likely a simple re-occurrence of the 1943 earthquake.

According to the post-tsunami surveys, the tsunami arrival time at the Totoral village, near the northern edge of the slip area (Fig. 1) where the maximum tsunami inundation height reached 10.8 m, was 6–10 min. This arrival time is shorter than for other tsunamigenic earthquakes in the Chilean subduction zone (ARÁNGUIZ *et al.* 2016). Numerical tsunami simulation suggests that this rapid tsunami propagation can be explained if the large slip patch is

close to the coastline and a narrow continental shelf and steep bathymetry are present (ARÁNGUIZ *et al.* 2016). Although the rupture front reaches the shallowest part near the trench in our source model (Fig. 3), the area of large slip concentrates at about 15–20 km depth on the fault plane close to the coast (Fig. 1). The occurrence of large slip near the coast in the second rupture episode may account for the shorter arrival time and large run-ups of tsunami near the northern edge of the source region.

5. Conclusion

We constructed the detailed seismic source model for the 2015 Illapel earthquake using the kinematic waveform inversion together with the HBP method. The model shows that the rupture unilaterally propagated northward in a gross sense, but in detail, we detected the two separated episodes of the rupture propagation near the hypocenter and the north of it, characterized by rupture propagation along the dip direction with variable rupture front velocities. High-frequency radiation sources tend to distribute at the deeper part of the slip, which is commonly observed for other subduction zone megathrust earthquakes. Gradual deceleration of rupture propagation, marked as the weak excitation of high-frequency radiation at the termination of slip, may reflect the gradual change of frictional property or stress state along the fault at the northern part of the Coquimbo-Illapel region. The integrated seismic source model from the high-frequency sources and the inverted slip should provide an opportunity to grasp the heterogeneous distribution of physical properties along the fault, which govern the diversity in earthquake rupture.

Acknowledgments

Teleseismic waveforms and the strong motion data from the networks; Antarctic Seismographic Argentinean Italian Network (AI), Canadian National Seismograph Network (CN), GEOSCOPE (G), Global Telemetered Seismograph Network (USAF/USGS, GT), Global Seismograph Network (GSN -

IRIS/IDA, II), Global Seismograph Network (GSN - IRIS/USGS, IU), and Red Sismologica Nacional (C1) are downloaded through the IRIS-DMC. Figures were generated with the Generic Mapping Tools (WESSEL and SMITH 1998). The authors thank Amato Kasahara and Bogdan Enescu for their valuable comments and suggestions. This work was supported by KAKENHI grant 24310133 from the Japan Society for the Promotion of Science. Chilean researchers would like to thank CONICYT grant FONDAP 15110017, FONDECYT 11140424 and the Chile-Japan Joint Project on Enhancement of Technology to Develop Tsunami Resilient Communities, sponsored by the Japan Science and Technology Agency (JST) and the Japan International Cooperation Agency through its SATREPS initiative. We acknowledge the editor and the two anonymous reviewers for their valuable comments and suggestions, which contribute to the significant improvement of the manuscript.

REFERENCES

- AKAIKE, H. (1980), *Likelihood and the Bayes procedure*, Trab. Estad. Y Investig. Oper. 31, 143–166. doi:10.1007/BF02888350.
- AMANTE, C. and EAKINS, B. (2009), ETOPO1 1 arc-minute global relief model: procedures, data sources and analysis, NOAA Tech. Memo. NESDIS NGDC-24. Natl. Geophys. Data Center, NOAA. doi:10.7289/V5C8276M.
- ARÁNGUIZ, R., GONZÁLEZ, G., GONZÁLEZ, J., CATALÁN, P.A., CIENFUEGOS, R., YAGI, Y., OKUWAKI, R., URRRA, L., CONTRERAS, K., DEL RIO, I. and ROJAS, C. (2016), *The 16 September 2015 Chile tsunami from the post-tsunami survey and numerical modeling perspectives*, Pure Appl. Geophys. 173, 333–348. doi:10.1007/s00024-015-1225-4.
- BECK, S., BARRIENTOS, S., KAUSEL, E. and REYES, M. (1998), *Source characteristics of historic earthquakes along the central Chile subduction* Askew et Alzone, J. South Am. Earth Sci. 11, 115–129.
- BERESNEV, I.A. (2003), *Uncertainties in finite-fault slip inversions: To what extent to believe? (A critical review)*, Bull. Seismol. Soc. Am. 93, 2445–2458. doi:10.1785/0120020225.
- BERNARD, P. and MADARIAGA, R. (1984), *A new asymptotic method for the modeling of near-field accelerograms*, Bull. Seismol. Soc. Am. 74, 539–557.
- CONTRERAS-REYES, E., BECERRA, J., KOPP, H., REICHERT, C., DÍAZ-NAVEAS, J. and CONTRERAS (2014), *Seismic structure of the north-central Chilean convergent margin: subduction erosion of a paleomagmatic arc*, Geophys. Res. Lett. 41, 1523–1529. doi:10.1002/2013GL058729.
- DEMETTS, C., GORDON, R.G. and ARGUS, D.F. (2010), *Geologically current plate motions*, Geophys. J. Int. 181, 1–80. doi:10.1111/j.1365-246X.2009.04491.x.
- ENGDAHL, E. and VILLASEÑOR, A. (2002), *41 Global seismicity: 1900–1999*. Int. geophys. 665–XVI doi:10.1016/S0074-6142(02)80244-3.
- FAN, W. and SHEARER, P.M. (2015), *Detailed rupture imaging of the 25 April 2015 Nepal earthquake using teleseismic P waves*, Geophys. Res. Lett. 42, 5744–5752. doi:10.1002/2015GL064587.
- FUKUYAMA, E. and MADARIAGA, R. (1998), *Rupture dynamics of a planar fault in a 3D elastic medium: rate- and slip-weakening friction*, Bull. Seismol. Soc. Am. 88, 1–17.
- GARDI, A., LEMOINE, A., MADARIAGA, R. and CAMPOS, J. (2006), *Modeling of stress transfer in the Coquimbo region of central Chile*, J. Geophys. Res. 111, B04307. doi:10.1029/2004JB003440.
- HARTZELL, S. and HEATON, T. (1983), *Inversion of strong ground motion and teleseismic waveform data for the fault rupture history of the 1979 Imperial Valley, California, earthquake*, Bull. Seismol. Soc. Am. 73, 1553–1583. <http://www.bssaonline.org/content/73/6A/1553.short>.
- HAYES, G.P., WALD, D.J. and JOHNSON, R.L. (2012), *Slab1.0: A three-dimensional model of global subduction zone geometries*, J. Geophys. Res. 117, B01302. doi:10.1029/2011JB008524.
- HOLTkamp, S. and BRUDZINSKI, M.R. (2014), *Megathrust earthquake swarms indicate frictional changes which delimit large earthquake ruptures*, Earth Planet. Sci. Lett. 390, 234–243. doi:10.1016/j.epsl.2013.10.033.
- HUSSEINI, M. (1975), *The fracture energy of earthquakes*, Geophys. J. Int. 43, 367–385.
- ISHII, M., SHEARER, P.M., HOUSTON, H. and VIDALE, J.E. (2005), *Extent, duration and speed of the 2004 Sumatra–Andaman earthquake imaged by the Hi-Net array*, Nature 435, 933–936. doi:10.1038/nature03675.
- KANEKO, Y., AVOUAC, J.-P. and LAPUSTA, N. (2010), *Towards inferring earthquake patterns from geodetic observations of interseismic coupling*, Nat. Geosci. 3, 363–369. doi:10.1038/ngeo843.
- KENNETT, B.L.N., ENGDAHL, E.R. and BULAND, R. (1995), *Constraints on seismic velocities in the earth from travel times*, Geophys. J. Int. 122, 108–124. doi:10.1111/j.1365-246X.1995.tb03540.x.
- KIKUCHI, M. and KANAMORI, H. (1991), *Inversion of complex body waves—III*, Bull. Seismol. Soc. Am. 81, 2335–2350.
- KOPER, K.D., HUTKO, A.R. and LAY, T. (2011), *Along-dip variation of teleseismic short-period radiation from the 11 March 2011 Tohoku earthquake (Mw 9.0)*, Geophys. Res. Lett. 38, L21309. doi:10.1029/2011GL049689.
- KRÜGER, F. and OHRNBERGER, M. (2005), *Tracking the rupture of the Mw = 9.3 Sumatra earthquake over 1,150 km at teleseismic distance*, Nature 435, 937–939. doi:10.1038/nature03696.
- LASKE, G., MASTERS, G., MA, Z. and PASYANOS, M. (2013), *Update on CRUST1.0 - A 1-degree global model of earth's crust*. EGU gen. assem. conf. abstr. 2658.
- LAY, T., KANAMORI, H., AMMON, C.J., KOPER, K.D., HUTKO, A.R., YE, L., YUE, H. and RUSHING, T.M. (2012), *Depth-varying rupture properties of subduction zone megathrust faults*, J. Geophys. Res. 117, B04311. doi:10.1029/2011JB009133.
- LEMOINE, A. and MADARIAGA, R. (2001), *Evidence for earthquake interaction in central Chile: the July 1997–September 1998 Sequence*, Geophys. Res. Lett. 28, 2743–2746. doi:10.1029/2000GL012314.

- LOMNITZ, C. (2004), *Major earthquakes of Chile: a historical survey, 1535-1960*, Seismol. Res. Lett. 75, 368–378. doi:[10.1785/gssrl.75.3.368](https://doi.org/10.1785/gssrl.75.3.368).
- MADARIAGA, R. (1977), *High-frequency radiation from crack (stress drop) models of earthquake faulting*, Geophys. J. R. Astron. Soc. 51, 625–651.
- MELGAR, D., FAN, W., RIQUELME, S., GENG, J., LIANG, C., FUENTES, M., VARGAS, G., ALLEN, R.M., SHEARER, P.M. and FIELDING, E.J. (2016), *Slip segmentation and slow rupture to the trench during the 2015, Mw8.3 Illapel, Chile earthquake*, Geophys. Res. Lett. 43, 961–966. doi:[10.1002/2015GL067369](https://doi.org/10.1002/2015GL067369).
- MÉTOIS, M., VIGNY, C., SOCQUET, A., DELORME, A., MORVAN, S., ORTEGA, I. and VALDERAS-BERMEJO, C.M. (2014), *GPS-derived interseismic coupling on the subduction and seismic hazards in the Atacama region, Chile*, Geophys. J. Int. 196, 644–655. doi:[10.1093/gji/ggt418](https://doi.org/10.1093/gji/ggt418).
- MORENO, M., ROSENAU, M. and ONCKEN, O. (2010), *2010 Maule earthquake slip correlates with pre-seismic locking of Andean subduction zone*, Nature 467, 198–202. doi:[10.1038/nature09349](https://doi.org/10.1038/nature09349).
- OHNAKA, M. and YAMASHITA, T. (1989), *A cohesive zone model for dynamic shear faulting based on experimentally inferred constitutive relation and strong motion source parameters*, J. Geophys. Res. 94, 4089. doi:[10.1029/JB094iB04p04089](https://doi.org/10.1029/JB094iB04p04089).
- OKUWAKI, R., YAGI, Y. and HIRANO, S. (2014), *Relationship between high-frequency radiation and asperity ruptures, revealed by hybrid back-projection with a non-planar fault model*, Sci. Rep. 4, 7120. doi:[10.1038/srep07120](https://doi.org/10.1038/srep07120).
- OLSON, A. and APSEL, R. (1982), *Finite faults and inverse theory with applications to the 1979 Imperial Valley earthquake*, Bull. Seismol. Soc. Am. 72, 1969–2001. <http://www.bssaonline.org/content/72/6A/1969.short>.
- PARDO, M., COMTE, D., MONFRET, T., BOROSCHEK, R. and ASTROZA, M. (2002), *The October 15, 1997 Punitaqui earthquake (Mw = 7.1): a destructive event within the subducting Nazca plate in the Central Chile*, Tectonophysics 345, 199–210. doi:[10.1016/S0040-1951\(01\)00213-X](https://doi.org/10.1016/S0040-1951(01)00213-X).
- RUIZ, S., MÉTOIS, M., FUENZALIDA, A., RUIZ, J., LEYTON, F., GRANDIN, R., VIGNY, C., MADARIAGA, R. and CAMPOS, J. (2014), *Intense foreshocks and a slow slip event preceded the 2014 Iquique Mw 8.1 earthquake*, Science 345, 1165–1169. doi:[10.1126/science.1256074](https://doi.org/10.1126/science.1256074).
- SPUDICH, P. and FRAZER, L. (1984), *Use of ray theory to calculate high-frequency radiation from earthquake sources having spatially variable rupture velocity and stress drop*, Bull. Seismol. Soc. Am. 74, 2061–2082.
- TASSARA, A. and ECHAURREN, A. (2012), *Anatomy of the Andean subduction zone: three-dimensional density model upgraded and compared against global-scale models*, Geophys. J. Int. 189, 161–168. doi:[10.1111/j.1365-246X.2012.05397.x](https://doi.org/10.1111/j.1365-246X.2012.05397.x).
- UDIAS, A., MADARIAGA, R., BUFORN, E., MUNOZ, D. and ROS, M. (2012), *The large Chilean historical earthquakes of 1647, 1657, 1730, and 1751 from contemporary documents*, Bull. Seismol. Soc. Am. 102, 1639–1653. doi:[10.1785/0120110289](https://doi.org/10.1785/0120110289).
- WALKER, K.T., ISHII, M. and SHEARER, P.M. (2005), *Rupture details of the 28 March 2005 Sumatra M w 8.6 earthquake imaged with teleseismic P waves*, Geophys. Res. Lett. 32, L24303. doi:[10.1029/2005GL024395](https://doi.org/10.1029/2005GL024395).
- WESSEL, P. and SMITH, W.H.F. (1998), *New, improved version of generic mapping tools released*, Eos, Trans. Am. Geophys. Union 79, 579–579. doi:[10.1029/98EO00426](https://doi.org/10.1029/98EO00426).
- YAGI, Y. and FUKAHATA, Y. (2011), *Introduction of uncertainty of Green's function into waveform inversion for seismic source processes*, Geophys. J. Int. 186, 711–720. doi:[10.1111/j.1365-246X.2011.05043.x](https://doi.org/10.1111/j.1365-246X.2011.05043.x).
- YAGI, Y. and OKUWAKI, R. (2015), *Integrated seismic source model of the 2015 Gorkha, Nepal, earthquake*, Geophys. Res. Lett. 42, 6229–6235. doi:[10.1002/2015GL064995](https://doi.org/10.1002/2015GL064995).
- YAGI, Y., NAKAO, A. and KASAHARA, A. (2012), *Smooth and rapid slip near the Japan Trench during the 2011 Tohoku-oki earthquake revealed by a hybrid back-projection method*, Earth Planet. Sci. Lett. 355–356, 94–101. doi:[10.1016/j.epsl.2012.08.018](https://doi.org/10.1016/j.epsl.2012.08.018).
- YAGI, Y., OKUWAKI, R., ENESCU, B., HIRANO, S., YAMAGAMI, Y., ENDO, S. and KOMORO, T. (2014), *Rupture process of the 2014 Iquique Chile earthquake in relation with the foreshock activity*, Geophys. Res. Lett. 41, 4201–4206. doi:[10.1002/2014GL060274](https://doi.org/10.1002/2014GL060274).
- YE, L., LAY, T., KANAMORI, H. and KOPER, K.D. (2016), *Rapidly estimated seismic source parameters for the 16 September 2015 Illapel, Chile M w 8.3 Earthquake*, Pure Appl. Geophys. 173, 321–332. doi:[10.1007/s00024-015-1202-y](https://doi.org/10.1007/s00024-015-1202-y).